

Optimizing data usage in regional body wave tomography by using asynchronous network data and relative sensitivity kernels: an example from Patagonia

Walid Ben-Mansour⁽¹⁾, Valerie Maupin⁽²⁾

¹Washington University in Saint Louis, Department of Earth, Environmental and Planetary Sciences, MO, US,

²PHAB – Centre for Planetary Habitability, Oslo, Norway

Corresponding author: walid@wustl.edu

This manuscript is not a non-peer reviewed preprint that has been submitted for publication in *Geophysical Journal International*. Subsequent versions of this manuscript may have different content. If accepted, the final version will be available via the Peer-reviewed Publication DOI link printed on the website link.

1 Optimizing data usage in regional body wave tomography by using
2 asynchronous network data and relative sensitivity kernels: an example from
3 Patagonia

4

5 Walid Ben-Mansour⁽¹⁾, Valerie Maupin⁽²⁾

6 1. Washington University in Saint Louis, Department of Earth, Environmental and Planetary
7 Sciences, MO, US,

8 2. PHAB – Centre for Planetary Habitability, Oslo, Norway

9 Abstract:

10

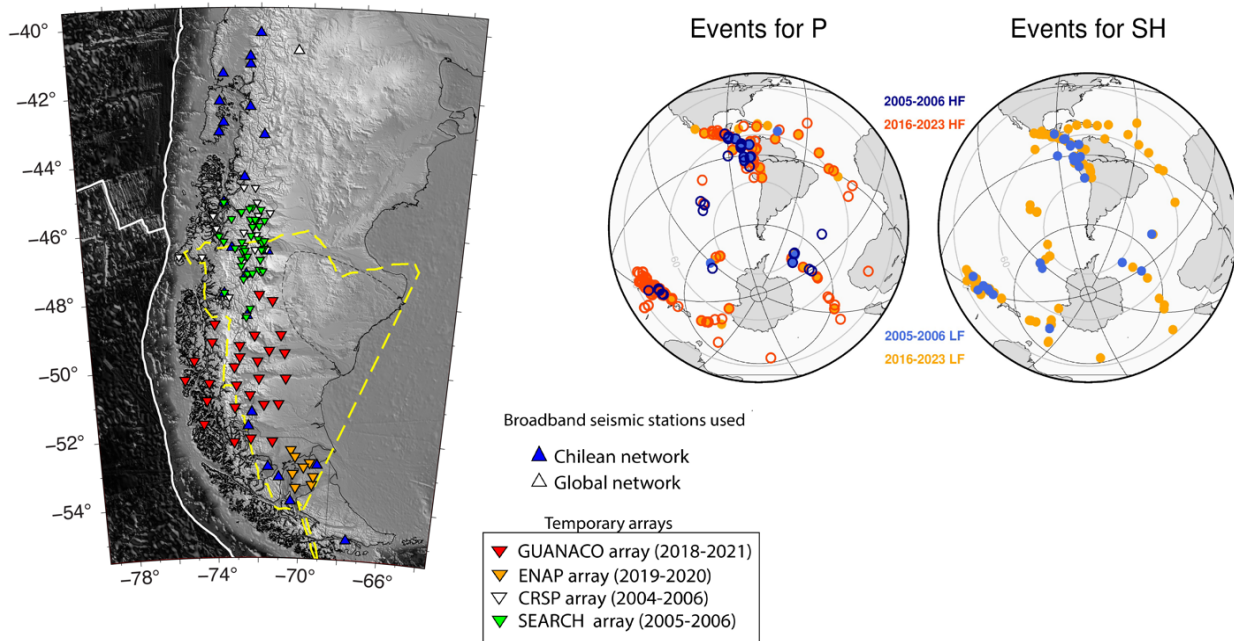
11 A very frequent approach for studying lithospheric processes is to deploy temporary seismological
12 networks in dedicated areas and to map the mantle structures with different approaches. One of
13 them is the well-established relative travel time body wave tomography. Different circumstances
14 often lead to a non-uniform deployment of stations both in space and time, and a wish to combine
15 data which have been acquired asynchronously. This is the situation in Patagonia where two
16 distinct seismic experiments provide complementary seismic data over the region covering the
17 Patagonia slab window. Combining these data in one regional relative body wave tomography is
18 however problematic as the two data sets are a priori with respect to two different reference
19 models. In this contribution, we show that the number of finite-frequency relative travel time
20 residuals varies very strongly from station to station for this data set, violating the assumption
21 implicit in relative travel time tomography of a unique reference model due to an even data
22 distribution for all events. We present how using relative sensitivity kernels allows us to solve this
23 problem and use all the data to produce a tomographic model. A resolution test proves how this
24 is crucial for resolving the important issue of the eastern extent of the slab window. In addition,
25 we discuss potential issues related to interference of the direct phases with core phases when
26 measuring finite-frequency travel time residuals by cross-correlation of waveforms in necessarily
27 relatively large time windows. We also briefly outline our preferred strategy for performing crustal
28 correction, keeping in mind that finite-frequency residuals require frequency-dependent crustal
29 corrections.

30 1. Introduction

31 Body wave tomography has given us a detailed picture of the 3-D structure of the mantle both at
32 global scale and at regional scale in different geodynamics settings. The increase in resolution in
33 recent models is due partly to novel methodologies based on full waveform inversion formulation
34 [Tromp et al. 2005; Fichtner et al., 2013; Tromp 2020], but also very importantly to the increase
35 in data availability through major data collection efforts (USArray, SinoProbe) and curation of
36 existing ones [Engdahl et al., 2020]. Although the resolution of global models is increasing,
37 regional models are still often superior in terms of resolution, justifying the common installation of
38 regional temporary networks for dedicated study of specific tectonic/geodynamical targets such
39 as the Alpine region with the AlpArray experiment [Hetenyi et al., 2018], Fennoscandia with
40 ScanArray [Thybo et al., 2020], or the Pyrenees with both PYROPE experiment [Chevrot et al.,
41 2017] and IberArray [Diaz et al. 2009]. These data are commonly exploited using standard
42 seismological techniques like surface-wave tomography, SKS-splitting analysis, receiver-function
43 analysis, and body-wave tomography. In the present paper, we would like to highlight how we
44 have overcome some of the challenges commonly encountered with data selection and
45 processing in regional body-wave tomography.

46
47 Regional body-wave tomography was introduced by Aki et al. (1977) and is still often referred as
48 ACH-tomography. Its main principle is to build a 3-D local model beneath a seismological network
49 by inversion of relative traveltimes between the stations, assuming errors in source times
50 locations and large-scale heterogeneities affect all travel times similarly and therefore cancel out
51 when measuring relative times. As very thoroughly detailed in Aki et al. (1977) and commonly
52 acknowledged, this results in models with unknown vertical average and where only relative
53 variations at a given depth should be interpreted. Another related point is that the model is with
54 respect to the average model beneath the network. As long as all events are recorded at almost
55 all stations, this is not an issue. When some stations are out-of-function for a longer period of
56 time, or record only a few events, it might become unclear if these stations should be included in
57 the data set or not, as the average model seen by the data will differ from event to event. An
58 extreme case is when different networks, covering different parts of the study region, have been
59 functioning at different times and therefore record different events. This is quite a common
60 situation, when data from different experiments done successively would benefit from being
61 combined.

62 This is the situation in Patagonia, at the southern end of the South American continent, where
 63 two temporary seismological networks were deployed, first in 2005-2006 over a region of about
 64 400 km by 200km size close to the present-day location of the Chilean triple junction (**Figure 1**)
 65 and in 2018-2021 to study the Patagonia slab window and the mantle properties beneath the
 66 Patagonia icefield in addition of new broadband seismic stations as part of the new permanent
 67 Chilean seismic network since 2015.



68
 69 **Figure 1.** *Topographic map of Southern Patagonia with broadband seismic stations used in this study.*
 70 *Teleseismic events used in the finite frequency body wave tomography. The events recorded by the early*
 71 *network (2006-2006) are shown in blue, with a full circle when used in the low-frequency range and with a*
 72 *darker blue open circle in the high-frequency range. The same in orange for the events recorded by the*
 73 *more recent network (2016-2023).*

74 Data from the earlier networks have been used in a regional scale P wave travel time tomography
 75 by [Russo et al \(2010\)](#) and [Miller et al. \(2023\)](#) showing the presence of low velocity anomaly
 76 between 46°S and 47°S associated with the slab window and fast velocity anomaly north to the
 77 Chilean triple junction associated with the Nazca slab. [Russo et al \(2010\)](#) also analyze shear
 78 wave splitting to interpret the upper mantle flow pattern associated with the slab window with
 79 ENE-WSW fast direction in the middle of the slab window and NE-SW trends south of the slab
 80 window. Recently, surface waves analysis [[Mark et al., 2022](#)] using the later network provided a
 81 better constraint on the southern extension of the slab window and a new regional scale crustal

82 model including both crustal thickness and new information on the thickness of the Australe-
83 Magallanes basins. Using later network and re-processing older networks for shear wave splitting
84 analysis, [Ben-Mansour et al. \(2022\)](#) show a strong E-W fast direction south of the Chilean triple
85 junction and the edge of the subducting Nazca slab. Most of south Patagonia show NE-SW fast
86 directions consistent with large-scale asthenospheric flow. A recent P-wave tomography by
87 [Kondo et al. \(2024\)](#) combines these data with ISC data and data from permanent stations to derive
88 a model at combined global and regional scale. In [Ben-Mansour et al. \(2025\)](#), we present the
89 results of a P and SH regional body-wave tomography done using a combination of data from the
90 two sets of networks and some permanent stations and discuss the geodynamic implications of
91 our findings.

92

93 In the present paper, we would like to present the methodological elements that we have
94 developed in the course of this tomographic analysis of asynchronous data, which can be of
95 general interest to the community. The core of the methodology to combine data from different
96 networks is to use relative kernels, which account for the data distribution individually for each
97 registered event, as introduced in [Maupin and Kolstrup \(2015\)](#). The efficacy of the methodology
98 was demonstrated with synthetic data in [Maupin \(2021\)](#), showing that combining asynchronous
99 temporary arrays in regional scale body wave tomography is not a trivial problem and tomography
100 may yield biased models if not conducted with relative sensitivity kernels. Relative kernels were
101 applied in [Veisi et al. \(2021\)](#). We confirm here their efficacy to combine asynchronous data by
102 analyzing the results of a real data case. We present first the data set that we have used and the
103 challenges related to its very uneven data distribution. Although relative kernels can be designed
104 using ray theory, we have worked with finite-frequency kernels. This implies measuring the
105 relative travel times in different frequency bands and allows us in particular to use rather low
106 frequencies also for P waves. We will present some examples of relative kernels and how they
107 allow us to include all the available data. Using finite frequency instead of picking arrival times,
108 interference of neighboring phases might bias the residuals for some epicentral distances and we
109 will discuss how we have addressed this issue. Some short elements concerning the frequency-
110 dependent crustal correction will also be presented.

111

112

113 2. Asynchronous datasets

114 Our data come from a very heterogeneous data set with twenty-two widely distributed permanent
115 stations, two compact early networks and a later deployment covering a larger region (**Figure 1**).
116 Combining those has the advantage of getting the bigger picture, still benefiting from the better
117 resolution offered by the more compact networks. Between 2004 and 2006, two broadband
118 seismic arrays (CRSP and SEARCH experiment) covering an area of 400 km by 400 km were
119 deployed north to the Chilean Triple Junction. The CRSP deployment provides the first
120 geophysical imaging of the slab window from body wave tomography and the mantle flow pattern
121 from shear wave splitting analysis [Russo et al., 2010]. The SEARCH experiment did not provide
122 any additional information on the geodynamic setting of this region but extended the seismic
123 model to the east. Between 2018 and early 2021, the deployment of twenty-six broadband
124 instruments south to the triple junction from 44°S to 53°S to bring new datasets in South Patagonia
125 allowed to map the southern extension of the slab window from surface wave tomography and
126 give a new crustal model [Mark et al., 2022]. Meanwhile, new broadband seismic stations were
127 deployed in Chile as part of the new permanent network since 2016 with twenty-two new seismic
128 stations between 40°S and 56°S. Four seismic stations were deployed in Tierra del Fuego by the
129 Empresa Nacional del Petróleo (ENAP) and provide an additional twelve months of data in 2019.
130 We also include the permanent station PLCA, part of the Global network, which provides
131 additional data between 2004 and 2006 and more recently between 2016 and 2023.

132

133 3. Selection of events and measurements of residuals

134

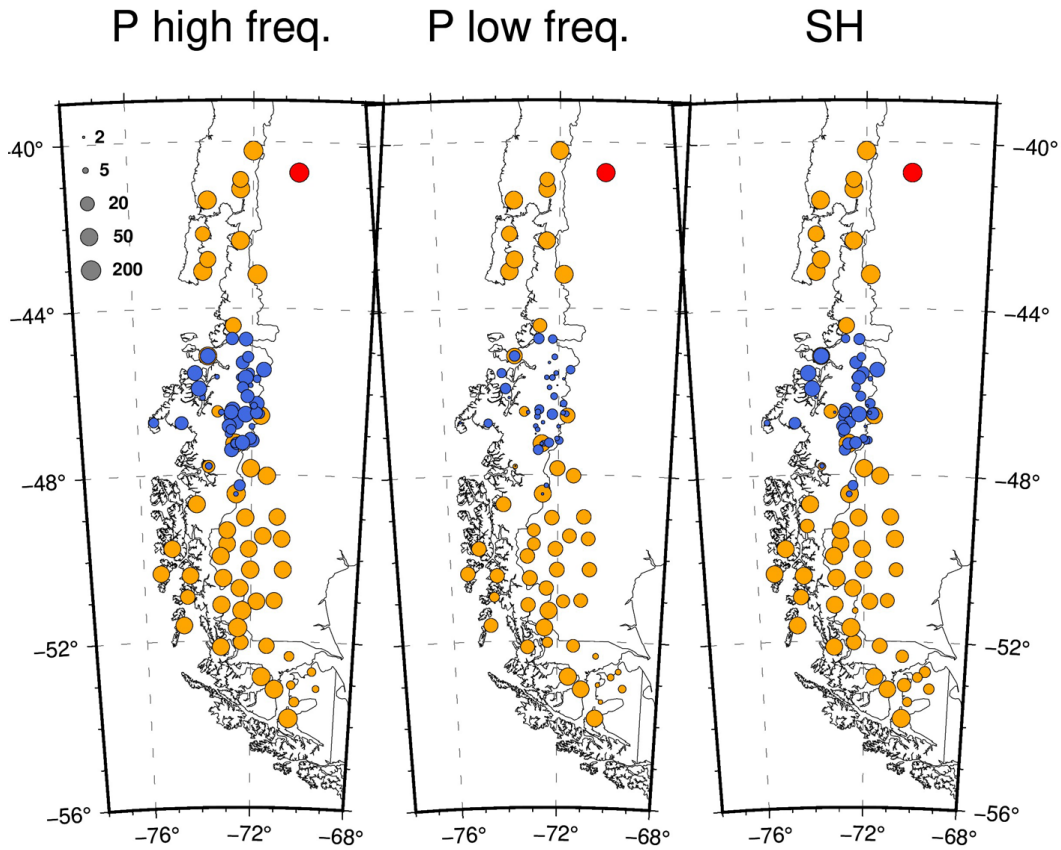
135 Relative finite-frequency travel time residuals were measured following mostly the procedure
136 described in Kolstrup and Maupin (2015), which combines the Iterative Cross-Correlation and
137 Stack (ICCS) algorithm of Lou et al. (2013) with the Multi-Channel Cross-Correlation method
138 (MCCC) of VanDecar and Crosson (1990). The ICCS algorithm calculates an array stack from
139 predicted arrival times, cross-correlates each seismogram with the array stack to find the time
140 lags at maximum cross-correlation. Each individual trace is aligned according to the time lag and
141 relative to the stack in an iterative procedure where the stack is updated for each iteration. After
142 alignment by ICCS, the cross-correlation coefficient and mean spectral coherence between each
143 trace and the stack are calculated. A weighted average of the two is computed and traces with a
144 value lower than a user-defined cut-off (usually about 0.5) are excluded. This procedure rejects

145 data with a significantly different shape than the array stack. The MCCC algorithm [VanDecar and
146 Crosson, 1990], used in the end on the already well-aligned traces, cross-correlates each possible
147 pair of seismograms and uses a least-squares method to calculate an optimized set of possibly
148 additional residuals. The additional residuals are in practice almost always negligible, but this
149 final step has the advantage of providing error-bars to each measurement to be used as weights
150 in the tomographic inversion.

151
152 We selected events larger than Mw5.4 in the epicentral range 28° and 98°. We band-pass-filter
153 waveforms around the secondary seismic noise peak ~0.2 Hz which dominates the signal. Here
154 we use two frequency bands for P but only one for S. Our experience is that two smaller frequency
155 ranges for S, as in Kolstrup and Maupin (2015), lead to more monochromatic waveforms and a
156 larger risk of cycle-skipping, but no clear benefit in amount of data. This is different from the P
157 wave where we see a clear benefit in using two frequency bands. Regardless of the fact that
158 these two frequency bands have different sensitivities to the structure, and therefore contribute
159 differently to the inversion, they also have a different noise level. Although the noise level is in
160 general lower in the high frequency range, it is not always the case. Some travel times which
161 could be measured only in the low frequency range were very useful for filling some azimuthal
162 gaps, data which would have been rejected with ray theory phase picking.

163
164 **Figure 2** shows the amount of data available at the different stations in the different frequency
165 bands, varying from 169 data at station PLCA for P waves in the high-frequency band down to 1
166 in a few cases. Some stations from the 2005-2006 network have a particularly low number of
167 detections, but this is compensated by the fact that they are closely spaced. By using relative
168 kernels, we can use all these data and do not need to discard some stations because they have
169 few data, or fair for a bias in resolution because the station density irregularity.

170



171
 172 **Figure 2.** Number of residuals having passed the selection criteria at the different stations for P waves
 173 (high and low frequency ranges), and for SH waves. In order to damp the dominance of the stations with
 174 many data, the size of the dots is proportional to $\text{atan}(N/10)$ where N is the number of residuals, as
 175 illustrated with grey dots on plot a. Blue dots correspond to stations from the early network, orange ones
 176 from the late network, and the red dot to permanent station PLCA which recorded during the whole period.

177

178 4. Relative kernels for Finite frequency body wave tomography

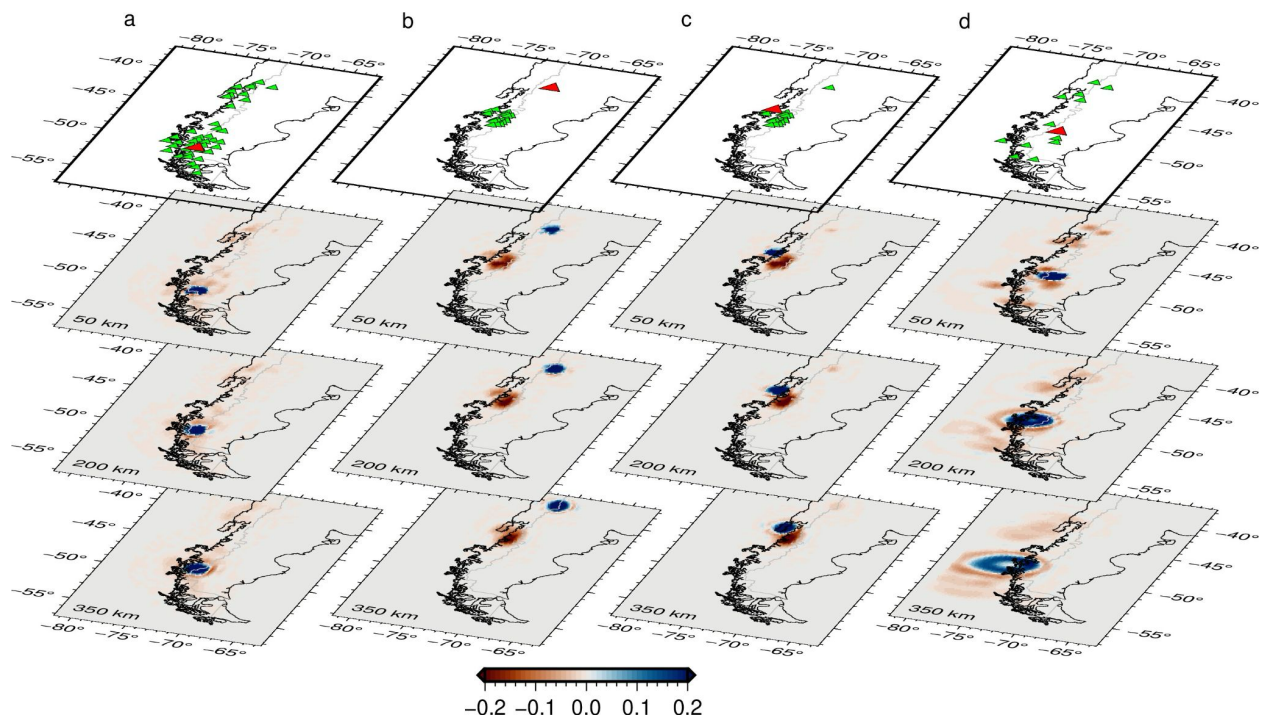
179 To solve the inverse problem from relative travel times to relative seismic velocity anomalies, we
 180 follow the data-adaptive, multiscale, finite-frequency tomography described in detail by [Hung et](#)
 181 [al. \(2011\)](#). This includes the computation of the 3-D Born-Fréchet (absolute) kernels which
 182 express the influence of velocity heterogeneities on finite-frequency travel times [[Dahlen et al.](#),
 183 [2000](#); [Hung et al. 2000](#); [Schmandt and Humphreys, 2010](#); [Maupin and Kolstrup, 2015](#)]. Our
 184 procedure has a simple additional step compared to previous studies corresponding to the
 185 computation of the relative kernels from the absolute ones. The relative kernels are simply the

186 absolute ones minus the average of the absolute kernels corresponding to data from a given
187 event. This ensures consistency with the data, which are by construction relative demeaned travel
188 times. We illustrate how they operate by plotting 4 examples in **Figure 3**.

189

190 The kernel in **Figure 3a** is associated with the P-wave residual at high frequency at station ES3R
191 for an event in Guatemala. The event was registered during the second period of station
192 deployment, with stations located in the North and South of the study region with a gap in
193 between. The kernel has large positive values beneath ES3R, but we can also notice negative
194 values spread in the whole region, corresponding to locations of stations that have registered the
195 same event. These negative values express that the residual measured at station ES3R is with
196 respect to the residuals measured at the other stations, and that its value therefore also depends
197 on the structure beneath these stations.

198



199

200 **Figure 3.** Relative sensitivity kernels for 3 cases of high-frequency P-wave data (plots a to c) and
201 one case of S-wave data (plot d). The upper panels show in red the station at which the data has
202 been recorded and in green the other stations having recorded the same event. The other panels
203 show the relative kernels at three selected depths with a color scale truncated at 20% of the
204 maximum value of the 3D kernel for better visualization.

205 **Figure 3b** shows the kernel for the residual at station PLCA for an event in Ecuador registered
206 during the early period of deployment, when station PLCA was supplemented by a network of
207 stations grouped close to 46°S. The positive kernel values beneath PLCA are associated with a
208 strong patch of negative values where the other stations are grouped. This expresses that the
209 relative residual at PLCA depends on the contrast in structure between this station and the region
210 further South. For the same event, the kernel of the residual at station AGU01, located in the
211 group of stations, is shown in **Figure 3c**. Although a small negative value is visible beneath PLCA,
212 this kernel dominantly expresses that the residual at AGU01 depends on the contrast in structure
213 between the region to the Northwest of the group of stations, where AGU01 is located, and the
214 rest of the region beneath the network.

215

216 **Figure 3d** shows an example of kernel for an SH wave recorded at station WIND. For this event
217 on the South Pacific Ridge, 13 residuals were measured at stations rather well distributed in the
218 whole region. This small number of residuals leads to a kernel with clear positive values beneath
219 WIND and rather clearly identified smaller negative values at the other stations having recorded
220 the event.

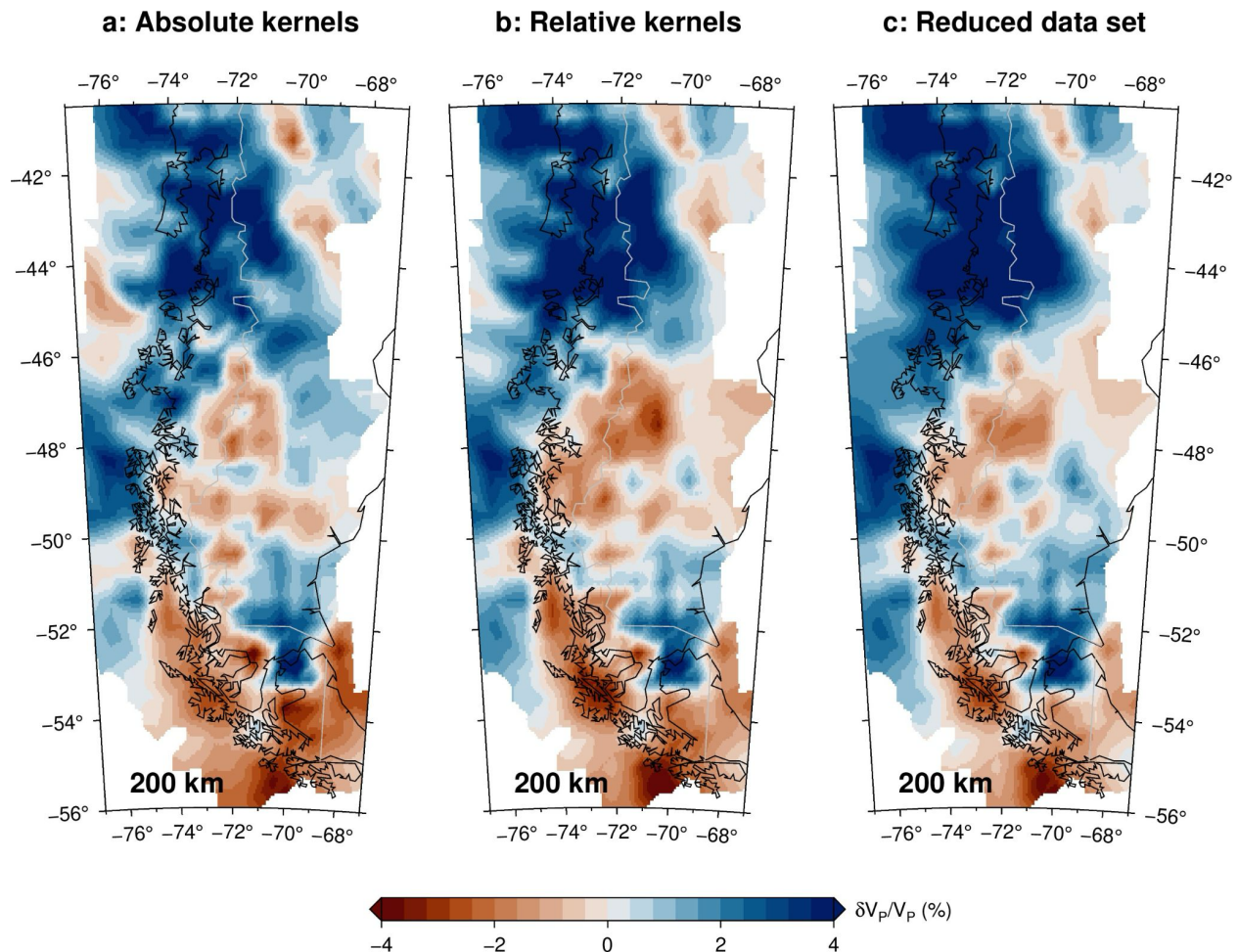
221 5. Comparison of tomographies with absolute and relative kernels

222 In order to study the influence of using relative kernels instead of absolute ones and to test the
223 resolution gained by adding data from the earlier networks, we have performed two tomographies
224 of the P-wave data in addition to the one done with all the data and the relative kernels, presented
225 in [Ben-Mansour et al. \(2025\)](#). In the first case, we use all the available data, but inverts with
226 absolute kernels instead of relative ones. In the other case, we use only data from the later
227 network, in orange in **Figure 2**. We refer to [Ben-Mansour et al. \(2025\)](#) for more details on the
228 parameters of the inversion and for a discussion of the model itself and its geodynamical
229 implications. We restrict ourselves here to an analysis of the differences between the three
230 models, shown at 200 km depth in **Figure 4**.

231

232 Although we do not combine data from different networks, we have still performed the inversion
233 of the reduced data set with relative kernels. This ensures that the differences we see are related
234 to the difference in the data set, and not in the methodology. In addition, even without combining
235 data from different networks, not all stations have good data for all events, and every event in

236 practice corresponds to a slightly different set of stations. This alone justifies using relative
237 kernels.
238



239
240 **Figure 4.** Maps at 200 km depth of P-wave models resulting from the inversion of the full data set
241 with absolute kernels (plot a), relative kernels (plot b), and (plot c) a data set reduced to late
242 events (2016-2023, see Figure 1).

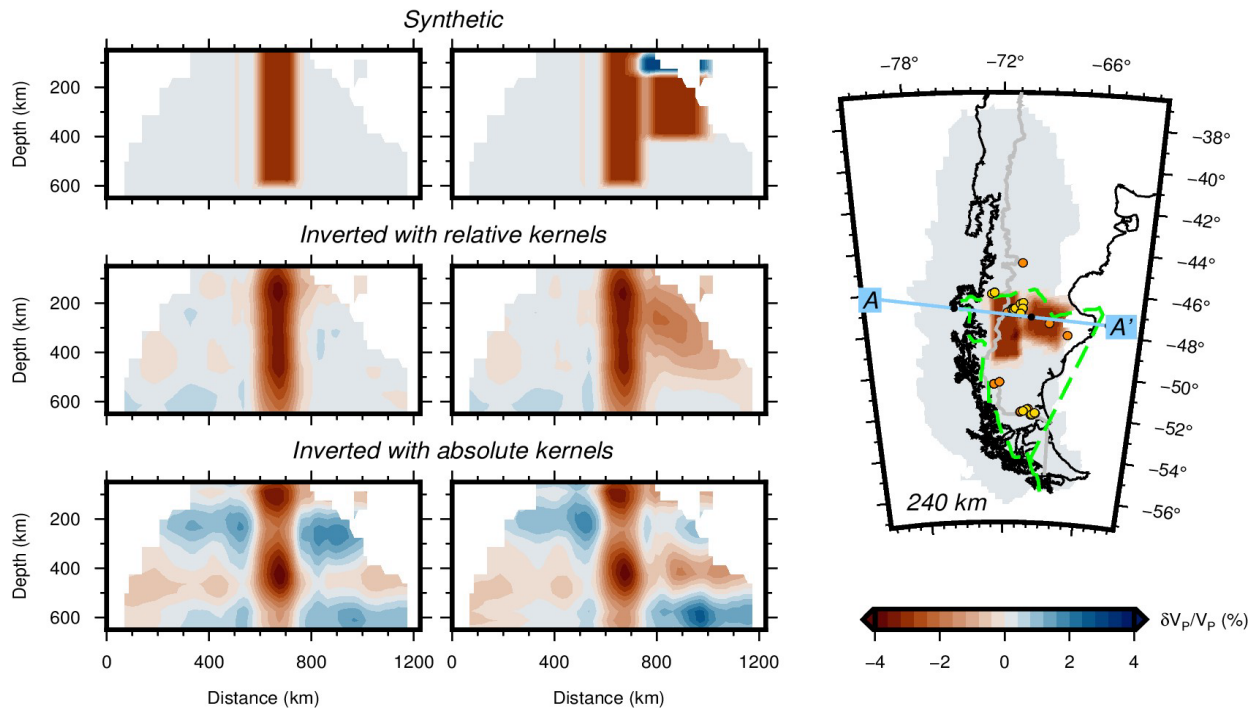
243 The differences between the models are not drastic, but still clearly visible. Keeping only the later
244 data provokes a data gap of about 2° at the southern end of the Nazca slab, in a region which is
245 crucial from a geodynamical point of view. This model (plot c) does not show a significant
246 degradation in the resolution of the area of the gap compared to the one using all data (plot b),
247 possibly because the major geodynamic boundary is by chance in the middle of the gap, a position
248 that would be favored by default by an inversion. The model has slightly stronger high velocities

249 and slightly weaker low velocities, corresponding to a slight change in the average model. As
250 noticed in [Maupin \(2021\)](#), models derived using relative kernels do not need to have zero mean,
251 but the average is not resolved by the data and should anyway not be interpreted. The model
252 including all data but using the absolute kernels for inversion (plot a), has more subdued large-
253 scale features compared with the model using relative kernels (plot b). This can best be seen in
254 the high-velocity region corresponding to the Nazca slab (42° to 46° S), and in the low-velocity
255 region at (48° S- 72° W). This is consistent with the results of the synthetic experiment in [Maupin](#)
256 [\(2021\)](#), showing that usage of relative kernels improves the large-scale rendering of the inversion.

257
258 Another noticeable difference between plots a and b in **Figure 4** is the presence of a negative
259 anomaly at about 69° S- 49° E in the inversion with relative kernels whereas it is positive in the
260 inversion with absolute ones. As this difference has potentially important implications for the
261 geodynamical interpretation of the model, we have examined its resolution with two synthetic tests
262 presented in **Figure 5**. The two models present two alternatives for the low-velocity zone
263 associated with the Patagonia slab window: a simple deep low-velocity anomaly or a low-velocity
264 zone also extending eastwards beneath a faster continental region at the surface. The inversion
265 with relative kernels is clearly able to resolve the difference between the two models even though
266 the area with high velocity at the surface is in a region with low resolution. The difference is far
267 less clear in the models derived with the absolute kernels. In general, these models are blurred
268 by extensive horizontally-lying anomalies. Between 200 and 300km depth, the low-velocity
269 anomaly is replaced by a high-velocity region, exactly as we observe in the model resulting from
270 the inversion of the data with absolute kernels (**Figure 4**, plot a).

271
272 Let us precise some technical elements of importance concerning the resolution tests. The
273 residuals are computed by combining the sensitivity kernels with the synthetic model but are also
274 demeaned event by event in order to simulate the actual data procedure. In addition, noise with
275 a standard variation of 0.04s, derived from data analysis, is added prior to inversion. As in **Figure**
276 **4**, the models are only shown in regions with resolution of at least 1% of the maximum of the
277 resolution matrix.

278
279



280
 281 **Figure 5: Resolution tests to compare inversion with relative and absolute sensitivity kernels. The**
 282 **synthetic models are shown in the two upper plots and in the map to the right-hand side. The map**
 283 **also shows the proposed contour of the Patagonia slab window as a green dashed line and the**
 284 **location of recent magmatism as orange dots. The middle and lower plots show the models**
 285 **resulting from inversions with relative and absolute kernels respectively.**

286 6. Choice of phases and interference with other phases

287 In addition to the discussion above concerning how to use data with irregular coverage, we would
 288 like to briefly discuss an additional element regarding quality control of finite-frequency residuals
 289 that we have not seen discussed in other studies. As opposed to ray-based tomography where
 290 data are usually individual phases arrival times picked at onset time, finite-frequency tomography
 291 relies on correlation of filtered traces which intrinsically have a finite time length. Measuring the
 292 residuals by cross-correlation of the waveforms with the stack assumes that all waveforms are
 293 similar. Any distance-dependent variation in the waveform would produce a bias. The method is
 294 therefore more prompt to bias by interference between phases than onset-time based tomography
 295 and possible biases should be checked carefully. Our procedure has an intrinsic iterative
 296 acceptance criterion based on the similarity of each waveform with the stack. This is efficient in

297 removing noisy individual waveforms but does not protect from biases due to gradually changing
298 waveforms due for example to interference with other phases than the phase of interest.

299

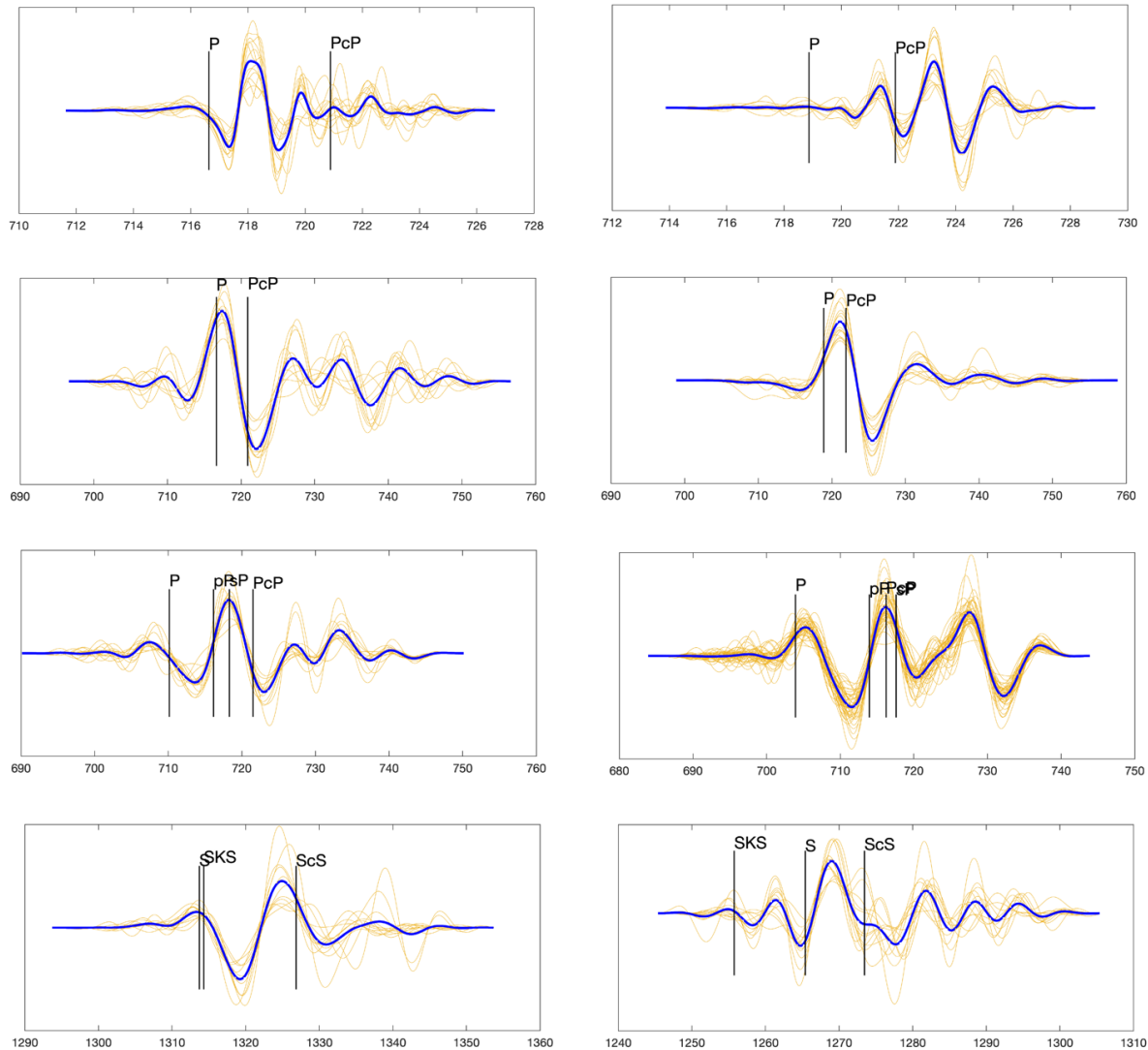
300 In the present study, we have used direct P and SH phases. As the region covered by the stations
301 is 14 degrees in its largest dimension, a small set of stations may fall out of this range for some
302 events and are then discarded. The lower epicentral limit is chosen to avoid the range where
303 direct waves have triplications and therefore complex waveforms. The higher limit ensures that
304 we do not include core-diffracted waves. We have tested if inclusion of core-diffracted phases P_{diff}
305 could provide additional data. Although our data are filtered in a rather narrow frequency range,
306 we observe that the shift in frequency content associated with getting further into the shadow
307 zone introduces a bias in the residuals beyond the acceptable noise level. The time windows used
308 to extract the data are of 20 and 70 seconds for the P waves at high and low frequencies
309 respectively and 70 seconds for S waves. These windows need to be long enough for the filters
310 to work satisfactorily. They may include other phases than the direct ones, in particular surface-
311 reflected phases and core-reflected phases at the largest distances. Concerning surface-reflected
312 phases, they interfere with the direct ones only for rather shallow events and have in these cases
313 very similar slowness values. We have therefore considered that the waveform does not change
314 significantly across the network, and that the slowness correction done when pre-aligning the data
315 are valid for direct as well as reflected phases. This has been verified manually and many of our
316 data are a combination of direct and surface-reflected waves, with the reflected ones dominating
317 in cases of favorable focal mechanisms.

318

319 The situation is rather different for the core-reflected phases which arrive shortly after the direct
320 phases which dive deep into the lower mantle. Despite similar paths, the difference in slowness
321 between the direct waves and the core-reflected ones is large enough to introduce errors in the
322 residuals if the core-reflected wave dominates the waveform. The amplitudes of the two waves
323 are however not totally independent. Since the waves depart from the source with very similar
324 angles of incidence, they have similar amplitudes at the source and their amplitude ratio is
325 dominantly related to the reflection coefficient at the CMB. This coefficient is smaller than 0.2 for
326 P waves in the epicentral distance range 80° to 90° [Rost and Thomas, 2010]. This implies that
327 the effect of the interference with the core-reflected phase should not be a major issue in most
328 cases for P waves. This is different for SH waves as they fully reflect at the CMB. In addition, they

329 may interfere with SKS waves. Also dominantly polarized as SV, SKS waves acquire a transverse
 330 component in cases of anisotropy, as for example observed in our study region [Ben-Mansour et
 331 al. 2022].

332



333

334 **Figure 6. Stack (blue lines) of data after alignment by ICCS (orange lines) for events in Fiji**
 335 **and Kermadec as a function of time (in seconds) annotated with the arrival times predicted**
 336 **by IASP91 at the center of the station network. The 2 upper plots are for P waves in the**
 337 **high-frequency range, those in the middle for P waves in the low-frequency range, and the**
 338 **bottom plots are for S waves. All cases shown on the left-hand side have been retained for**
 339 **inversion, while those on the right-hand side have been rejected.**

340 We have therefore introduced a rejection criterion in our data selection procedure. Events with a
341 maximum amplitude of the stack arriving after the theoretical arrival of the core-reflected are
342 automatically rejected. All other events which have core-reflected phases arriving within the
343 selected time window are visually inspected before acceptance. **Figure 6** shows examples of
344 selected and rejected data. For our data set, rejection of possibly core-phase biased events is not
345 a major problem for P waves since they mostly belong to the Kermadec-Tonga-Fiji area where
346 the seismicity is plentiful For S waves, the selection is more difficult to do and interference with
347 core phases may add noise in the data. In any case, we recommend attention to this potential
348 issue and careful inspection of the waveforms.

349

350 7. Crustal correction

351 The near-vertical incidence of the direct P and SH waves used in general in regional body-wave
352 tomography does not allow for resolving the crust, but variations in Moho depth and topography
353 across the network affect the residuals and need to be accounted for. In regions where the crustal
354 structure is too poorly known, one can assume that the crust affects the residuals in the same
355 way for all events and contributes as a station term which can be inverted for during the
356 tomography (e.g. [Civiero et al., 2016](#)). However, the most common practice is to correct for the
357 crust using a global model such as CRUST1.0 [[Laske et al., 2013](#)] or a regional model. In
358 Patagonia, we were able to use the regional crustal model from [Mark et al. \(2022\)](#), as presented
359 in [Ben-Mansour et al. \(2025\)](#).

360 It is well-established that the reverberations in the crust affect the travel times at different
361 frequencies in different ways, and that crustal delay times of high-frequency and low-frequency
362 data may be significantly different, in particular in oceanic domains and regions of thick
363 sedimentary basins [[Yang and Shen, 2006](#); [Ritsema et al., 2009](#); [Kolstrup and Maupin, 2015](#)].
364 The crustal correction of finite-frequency travel time residuals should therefore be made frequency
365 dependent. This is done in our study following the procedure of [Kolstrup and Maupin \(2015\)](#) which
366 uses the reflectivity method [[Levin and Park, 1997](#)] applied in a 1-D seismic model below each
367 station. An important point is that it is advantageous to perform the correction by appropriately
368 shifting the time series with respect to each other before performing the stacking and cross-
369 correlation procedure. There are two main reasons for that. Firstly, by correcting for known delays,
370 we minimize the time differences between the time series, reducing the risk of cycle skipping, and

371 ensuring a faster convergence of the stack. A second point, which is less obvious but nonetheless
372 important, is that relative body wave tomography assumes that the mean of the residuals for every
373 event is zero. Conducting crustal correction after measuring the residuals is likely to change the
374 mean of the data set, requiring further adjustment of the residuals, a pretty unnecessary
375 complicating step.

376 8. Discussion and conclusion

377
378 The advantage of combining data from different networks will vary from case to case. Often it will
379 be a matter of extending the region of study. In the present case, it is a matter of getting the big
380 picture in addition to a better resolution in a region of particular interest from a geodynamical point
381 of view. We see for example that with our data coverage using the relative kernels is crucial for
382 imaging the eastward extension at depth of the Patagonia slab window, which is of major
383 geodynamical interest.

384
385 Instead of using relative kernels, one can invert the differences in residuals between pairs of
386 stations. This also allows combining data that have not been registered at all stations
387 simultaneously. This procedure was chosen by [Kondo et al. \(2024\)](#) for a P-wave data set partly
388 overlapping with the one we use here. The kernels to be used in that case are then just the
389 difference between the two absolute kernels of the pair of stations involved [[Hung et al., 2000](#)].
390 The main disadvantage of this method is to increase the size of the inverse problem since the
391 number of data points per event is basically the square of the number of original residuals, without
392 actually increasing the information content. Depending on how the residuals are calculated, one
393 also loses the great advantage of MCCC where the compatibility of the residual differences
394 between pairs of stations is used for data quality analysis and error bar assignment.

395
396 We have also presented which selection criteria we have used to avoid bias in data by interference
397 with core phases at large epicentral distances. Due to the length of the time windows on which
398 we have to operate, using low-frequency data is more challenging than using high-frequency data
399 or picking arrival times. This is particularly true for S wave data at epicentral distances close to
400 the shadow zone. The quality of the inverted model is totally dependent on a correct selection of
401 the data on which to measure residuals. Although we experience that the ICCS algorithm is very

402 efficient in removing noisy traces and cases with incoherent waveforms, an automatic procedure
403 is not able to deal with all cases and manual review of all data is an advantage.

404

405 Although regional body-wave tomography only provides relative velocity anomalies, it is a popular
406 method for exploiting data from numerous seismological station deployments. Especially in
407 association with surface wave studies, it can provide the resolution necessary to answer intricate
408 geodynamical questions difficult to address with global models. In this paper, we have shared
409 some recommendations for data processing and inversion gained through our experiences with
410 a tomography of Patagonia and shown in particular that data from asynchronous networks can
411 be combined and that usage of relative sensitivity kernels is important to avoid biases in the
412 models.

413

414 Acknowledgements

415

416 The authors would like to thank Christine Thomas, University of Munster, for advice concerning
417 interference of direct waves with core phases. The computations have been made using a
418 modified version of the software for finite-frequency body wave tomography kindly provided by
419 Shu-Huei Huang, National Taiwan University. Waveforms and metadata were accessed via the
420 EarthScope Data Management System. This research was funded by the National Science
421 Foundation under grant EAR-1714154: Collaborative Research: Solid Earth Response of the
422 Patagonian Andes to Post-Little Ice Age Glacial Retreat. VM is supported by the Research
423 Council of Norway's project 332523 (Center for Planetary Habitability). Figures were produced
424 using GMT software [Wessel et al., 2013] using perceptually uniform colour maps generated by
425 Fabio Cramer [Cramer, 2018] and available at <http://www.fabiocramer.ch/colourmaps.php>.

426

427 Data availability

428 Data used in this study are from the temporary seismic networks GUANACO, SEARCH and CRSP
429 temporary seismic networks respectively under the network code 1P, YJ and XJ. Permanent
430 stations from the Chile network and Global network are under the network code C/C1 and GT.
431 Data can be obtained from the EarthScope data center:

432 1P : https://www.fdsn.org/networks/detail/1P_2018/,

433 XJ: https://www.fdsn.org/networks/detail/XJ_2004/,

434 YJ: https://www.fdsn.org/networks/detail/YJ_2004/,

435 C: <https://www.fdsn.org/networks/detail/C/>,

436 C1: <https://www.fdsn.org/networks/detail/C1/>

437 GT: <https://www.fdsn.org/networks/detail/GT/>).

438

439 References

440 Aki, K, Christoffersson, A, Husebye, E (1977), Determination of the three-dimensional seismic
441 structure of the lithosphere, *Journal of Geophysical Research*, 82 ,2, 277--296.

442

443 Ben-Mansour, W, Wiens, DA, Mark, HF, Russo, RM, Richter, A, Marderwald, E, Barrientos, S
444 (2022), Mantle flow pattern associated with the Patagonian slab window determined from
445 azimuthal anisotropy, *Geophysical Research Letters*, 49,18, e2022GL099871.

446

447 Ben-Mansour, W., Maupin, V, Wiens, DA, Richter, A (2025), Deep source regions for Patagonia
448 backarc volcanism imaged by finite frequency body wave tomography, *EarthArxiv*,
449 <https://doi.org/10.31223/X5XF08>.

450

451 Chevot S, Sylvander, M, RESIF (2017), Seismic network X7: PYROPE PYRenean Observational
452 Portable Experiment, <https://doig.org/10.15778/RESIF.X72010>.

453

454 Civiero, C, Goes, S, Hammond, JOS, Fishwick, S, Ahmed, A, Ayele, A, Doubre, C, Goitom, B,
455 Keir, D, Kendall, JM, Leroy, S, Ogubazghi, O, Rumpker, G, Stuart, GW (2016), Small-scale
456 thermal upwellings under the northern East African Rift from S travel time tomography, *Journal*
457 *Geophysical Research, Solid Earth*, 121, 7395–7408, doi:10.1002/2016JB013070.

458

459 Crameri, F (2018). Scientific colour maps: perceptually uniform and colour-blind friendly, doi:
460 10.5281/zenodo.1243862, code repository at www.fabiocrameri.ch/colourmaps

461

462 Dahlen, FA , Hung, S-H, Nolet, G (2000), Frechet kernels for finite-frequency traveltimes—I.
463 Theory, *Geophysical Journal International*,141,1,157—174.
464

465 Diaz, J, Villasenor, A, Gallart, J, Morales, J, Pazos, A, Cordoba, D, Pulgar, J, Garcia-Lobon, JL,
466 Harnafi, M and others (2009), The IBERARRAY broadband seismic network: a new tool to
467 investigate the deep structure beneath Iberia ,*Orfeus Newsletter*,8,2, 1—6.
468

469 Engdahl E.R, Di Giacomo D., Sakarya B., Gkarlaouni C. G., Harris J., Storchak D. A.,2020. ISC-
470 EHB 1964–2016, an Improved Data Set for Studies of Earth Structure and Global Seismicity,
471 *Earth and Space Science*, Vol 7, e2019EA000897.
472

473 Fichtner, A, Trampert, J, Cupillard, P, Saygin, E, Taymaz, T, Capdeville, Y, Villasenor, A (2013),
474 Multiscale full waveform inversion, *Geophysical Journal International*, 194, 1,534—556.
475

476 Hetenyi, G, Molinari, I, Clinton, J, Bokelmann, G, Bondar, I, Crawford, WC, Dessa, JX, Doubre,
477 C, Friederich, W, and Fuchs, F, and others (2018), The AlpArray seismic network: a large-scale
478 European experiment to image the Alpine Orogen, *Surveys in geophysics*,39,1009—1033.
479

480 Hung, S-H and Dahlen, FA and Nolet, G. (2000), Frechet kernels for finite-frequency traveltimes:
481 II. Examples, *Geophysical Journal International*, 141, 1,175--203.
482

483 Hung, SH, Chen, WP, Chiao, LY (2011), A data-adaptive, multiscale approach of finite-frequency,
484 traveltome tomography with special reference to P and S wave data from central Tibet, *Journal of*
485 *Geophysical Research: Solid Earth*, 116, B6.
486

487 Kolstrup M.L. and Maupin, V. (2015), Measuring and crust-correcting finite-frequency travel time
488 residuals – application to southwestern Scandinavia, *Solid Earth*, 6, 1117-1130.
489

490 Kondo, Y, Obayashi, M, Sugioka, H, Shiobara, H, Ito, A, Shinohara, M, Iwamori, H, Kinoshita, M,
491 Miller, M, Tassara, C, Ojeda, J (2024), Seismic image of the central to southern Andean
492 subduction zone through finite-frequency tomography, *Journal of Geophysical Research: Solid*
493 *Earth*, 129,11.

494 Laske, G, Masters, G, Ma, Z, Pasyanos, M (2013), Update on CRUST1. 0- A 1-degree global
495 model of Earth's crust,,Geophysical research abstracts,15,15,2658.
496

497 Levin, V and Park, J (1997), P-SH conversions in a flat-layered medium with anisotropy of
498 arbitrary orientation, Geophysical Journal International, 131,2, 253--266.
499

500 Lou, X, Van Der Lee, S, Lloyd, S (2010), AIMBAT: A python/matplotlib tool for measuring
501 teleseismic arrival times, Seismological Research Letters, 84, 1, 85--93.
502

503 Maupin, V, Kolstrup, ML (2015), Insights in P-and S-wave relative travelttime tomography from
504 analysing finite-frequency Frechet kernels, Geophysical Journal 202, 3,1581--1598.

505 Maupin, V (2021), Combining asynchronous data sets in regional body-wave tomography,
506 Geophysical Journal International, 224,1, 401--415.
507

508 Mark, HF, Wiens, Douglas A, Ivins, Erik R, Richter, A, Ben-Mansour, W, Magnani, MB,
509 Marderwald, E, Adaros, R, Barrientos, S (2022), Lithospheric erosion in the Patagonian slab
510 window, and implications for glacial isostasy, Geophysical Research Letters, 49, 2,
511 e2021GL096863.
512

513 Miller, M, Priestley, K, Tilmann, F, Bataille, K, Iwamori, H (2023), P wave teleseismic tomography
514 of the subducted Chile rise, Journal of South American Earth Sciences, 128, 104474.
515

516 Ritsema, J, Van Heijst, HJ, Woodhouse, JH, Deuss, A (2009), Long-period body wave travel
517 times through the crust: implication for crustal corrections and seismic tomography, Geophysical
518 Journal International, 179, 2,1255--1261.
519

520 Rost S and Thomas C (2010). High resolution CMB imaging from migration of short-period core
521 reflected phases, Phys. Earth planet. Int., 183, 143-150, doi:10.1016/j.pepi.2010.04.005.

522 Russo, RM (2010), Subduction of the Chile Ridge: Upper mantle structure and flow, Gsa
523 Today,20.
524

525 Schmandt, B and Humphreys, E (2010), Seismic heterogeneity and small-scale convection in the
526 southern California upper mantle, *Geochemistry, Geophysics, Geosystems*, 11,5.
527

528 Thybo, H, Bulut, N, Grund, M, Mauerberger, A, Makushkina, A, Artemieva, IM, Balling, N,
529 Gudmundsson, O, Maupin, V, Ottemoller, L, Ritter, J, Tilmann, F (2021), ScanArray—A
530 Broadband Seismological Experiment in the Baltic Shield, *Seismological Research Letters* 92 (5):
531 2811–2823.
532

533 Tromp, J, Tape, C, Liu, Q (2005) Seismic tomography, adjoint methods, time reversal and
534 banana-doughnut kernels, *Geophysical Journal International*, 160, 1, 195, 216.

535 Tromp, J (2020), Seismic wavefield imaging of Earth’s interior across scales, *Nature Reviews*
536 *Earth & Environment*, 1, 1, 40-53.
537

538 VanDecar, JC and Crosson, RS (1990), Determination of teleseismic relative phase arrival times
539 using multi-channel cross-correlation and least squares, *Bulletin of the Seismological Society of*
540 *America*, 80,1, 150--169.
541

542 Wessel, P., Smith, W., Scharroo, R., Luis, J. , Wobbe, F., (2013). Generic Mapping Tools:
543 improved version released, *EOS, Trans. Am. geophys. Un.*, 94, 409–410.
544

545 Veisi, M, Sobouti, F, Chevrot, S, Abbasi, M, Shabaniyan, E (2021), Upper mantle structure under
546 the Zagros collision zone; insights from 3D teleseismic P-wave tomography, *Tectonophysics*, 819,
547 229106.
548

549 Yang, T and Shen, Y (2006), Frequency-dependent crustal correction for finite-frequency seismic
550 tomography, *Bulletin of the Seismological Society of America*, 96, 6 ,2441--2448.